Multiple pulses of fluids involved in the formation of carbonatite-related REE deposits as revealed by fluorite

Shilin Li [a,b], Wei Zhang [c,*], Jiali Cai [a], Fangyue Wang [d], Wei Terry Chen [a,b,*]

[a] State Key Laboratory of Ore Deposit Geochemistry, Institute of Geochemistry, Chinese Academy of Sciences, Guiyang 550081, China
[b] University of Chinese Academy of Sciences, Beijing 100049, China
[c] School of Earth Sciences, Yunnan University, Kunming 650500, China
[d] Ore Deposit and Exploration Centre, School of Resources and Environmental Engineering, Hefei University of Technology, Hefei 230009, China

ABSTRACT

Formation of carbonatite-related REE deposits generally associated with hydrothermal fluids exsolved from carbonatite melts. Deciphering the nature and evolution of the fluids is critical for establishing ore-formation models, and was mostly benefited from multi-analytical investigation of specific minerals presenting in multi-generation veins. However, there is a risk that the minerals in specific-generation veins not always precipitated solely from the single-stage fluids particularly for a dynamic mineralizing system. In order to evaluate this potential risk, this study conducted a combined textural, in situ trace elemental and fluid inclusion investigation of fluorite from multiple generations of veins in the Muluozhai carbonatite-related REE deposit, SW China. The veins dominate the mineralization system of the deposit, and include four generations/stages: fenitization (Stage I), pre-REE (Stage II), early REE (Stage III) and late REE (Stage IV) stages in which the ore minerals are all dominated by bastnäsite. Fluorite grains are widely present in these generations of veins, but high-resolution CL imaging reveal that most of them display complex internal textures composed commonly of core, mantle and rim domains from center outward. These domains exhibit different CL-intensities that are well correlated with chemical compositions and even types of fluid inclusions they hosted. This study confirmed that the "core-mantle-rim" textures of fluorite are essentially responses to interaction of early grains (i.e., represented by cores) with multi-stage fluids through dissolution-reprecipitation processes. Trace elemental and fluid-inclusion microthermometric results show that the cores (also for mantles or rims) in fluorite from Stages I to III veins have comparable REE concentrations and patterns and homogenization temperatures of fluid inclusions, strongly suggesting that the core-mantle-rim fluorite grains in these veins are originally formed at Stage I, and were variably captured or metasomatized by fluids of Stage II or III during development of these generations of veins. Similar core-mantle-rim fluorite grains are also present in Stage IV veins, and thus are constrained to be also "xenocrysts" formed in a similar manner. They are surrounded or even locally disturbed by a number of euhedral and/or slightly oscillatory fluorite grains which are supposed to be formed from a different manner. On the basis of their close association with bastnäsite and relatively high homogenization temperatures of fluid inclusions they host, we proposed that these euhedral fluorite grains are products of Stage IV fluids.

Clear understanding of the internal textures and paragenesis of fluorite allows us to propose a genetic model for the Muluozhai deposit that the REE mineralization in Stages III and IV involves likely different pulses of carbonatite-related REE-rich fluids, and REE deposition was possibly mainly triggered by incursions of external fluids (e.g., meteoric water). This study also highlights that the phenomenon regarding presences of early-stage "xenocrysts" in late-generation veins of carbonatite-related vein systems may be more common than previously thought, and thus investigation in a textural context is critical for deciphering ore genesis.

* Corresponding authors at: State Key Laboratory of Ore Deposit Geochemistry, Institute of Geochemistry, Chinese Academy of Sciences, Guiyang 550081, China (W. Terry Chen).
E-mail addresses: zhangwei1988@ynu.edu.cn (W. Zhang), chenwei@mail.gyig.ac.cn (W. Terry Chen).

1. Introduction

As the most important providers of REEs in the world, carbonatite-related REE deposits have long been the attractive targets for research and exploration (e.g., Sheard et al., 2012; Verplanck et al., 2016; Simandl and Paradis, 2018). It is generally accepted that the major economic REE hosts such as bastnäsite and monazite are able to be either crystallized directly from carbonatite melts or precipitated from REE-fertile fluids expelled from carbonatite melts. However, the former was rarely documented (such as the Mountain Pass deposit, California, USA; Castor, 2008), partially due to the fact that the bastnäsite is

unstable in high temperatures (Gysi and Williams-Jones, 2015), whereas the latter was more commonly confirmed to be critical for formation of some giant REE deposits such as the Maoniuping, Bachu and Weishan deposits in China (Xie et al., 2009; Cheng et al., 2018; Jia and Liu, 2020), Wicheeda and Ashram deposits in Canada (Trofanenko et al., 2016; Beland and Williams-Jones, 2021), and Songwe Hill deposit in Malawi (Broom-Fendley et al., 2017). In these deposits, the REE mineralization is commonly characterized by development of vein systems. Studies of these deposits demonstrated that the carbonatite-expelled REE-rich fluids are generally sulfate-rich (Walter et al., 2017, 2020; Wan et al., 2021; Zhang et al., 2022), and final deposition/mineralization of REEs
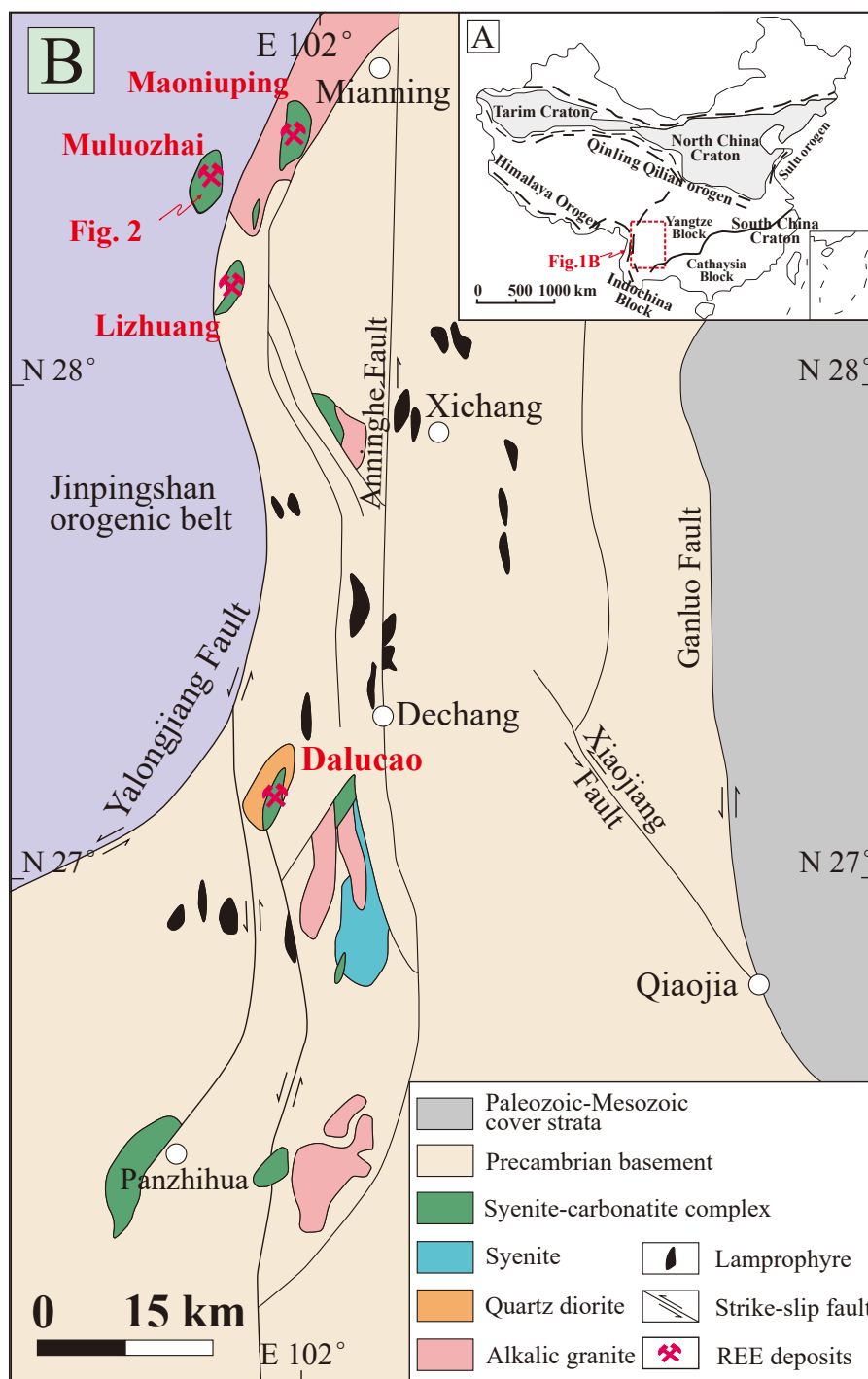

Fig. 1. (A) Overview of the tectonic regions of China. (B) Regional tectonic map of the Mianning-Dechang REE metallogenic belt, also shown is the location of representative REE deposits (modified from Yuan et al., 1995).

likely involved a number of processes such as fluid immiscibility, fluid mixing or fluid-rocks interaction (Williams-Jones and Palmer, 2002; Migdisov and Williams-Jones, 2014). In the past decade, deciphering the potential roles of these processes on ore formation was generally benefited from chemical and isotopic investigation of specific minerals (as well as the fluid inclusions they host) presenting in multi-stage veins (Xu et al., 2012; Shu et al., 2020; Zheng and Liu, 2019; Shu et al., 2020; Zhang et al., 2021; Zheng et al., 2021). In most cases, however, the candidate minerals in veins of a specific stage are not essentially the ones formed in a single stage, but instead exhibit complex internal textures indicative of multiple incursion/overprints of fluid. As such, the obtained chemical, isotopic compositions and even temperatures (e.g., fluid inclusions) from minerals have risks of exhibiting unreasonably variations even in a single grain.

In order to evaluate the potential risks mentioned above, this study conducted a combined textural, trace elemental and fluid inclusion investigation on the fluorite in the Muluozhai carbonatite-related REE deposit in the Mianning-Dechang (MD) REE metallogenic belt, SW China. Fluorite is indeed a good candidate as it is a common gangue mineral in carbonatite-related REE deposits, and is able to be present throughout the whole history of deposit formation (Beland and Williams-Jones, 2021; Liu and Hou, 2017; Smith and Henderson, 2000; Zhang et al., 2022). It was also well shown that both the textures and chemistry of fluorite are sensitive to physicochemical conditions of fluids and was widely used to decipher mineralizing processes of hydrothermal deposits (Gagnon et al., 2003; Schwinn and Markl, 2005; Xu et al., 2012; Assadzadeh, et al., 2017; Duan et al., 2022). In addition, fluorite is also a good host for fluid inclusions (Xie et al., 2009; Zheng and Liu, 2019; Shu et al., 2020; Zhang et al., 2022), thus allowing to evaluate the nature of the parental fluids in a textural context (e.g., Möller et al., 1976; Hill et al., 2000; Bau et al., 2003; Sallet et al., 2005; Deng et al., 2014; Schlegel et al., 2020; Duan et al., 2022). The new dataset further allows us to comprehensively constrain the nature of potentially multiple pluses of fluids recorded in fluorite, and further providing new insights on potential tools constraining mechanism of REE mineralization in carbonatite-related REE deposits.

2. Geological background

2.1. Regional geology

The Mianning-Dechang REE metallogenic belt, 270 km in length and 15 km in width, is situated in the western margin of the Yangtze Block in South China (Fig. 1A). It is bordered by the Yalongjiang fault to the west and Anninghe fault to the east (Fig. 1B). The basement in the belt is mainly composed of Archean high-grade metamorphic and Proterozoic meta-sedimentary rocks, and covered by Paleozoic-Mesozoic clastic-carbonate and mid-Permian flood basalt sequences (Cong, 1988; Luo et al., 1998). The collision between India and Asia continents affected the western margin of the Yangtze Craton and resulted in the formation of the N-S trending Jinpingshan Orogen (Fig. 1B) (Luo et al., 1998; Yin and Harrison, 2000; Zhong et al., 2001; Hou and cook, 2009). A series of strike-slip faults were developed to accommodate the stress and strain from the collision and are responsible for extensive magmatism e. g., potassium-rich alkaline rocks, lamprophyres and carbonatites (Wang et al., 2001; Guo et al., 2005; Hou et al., 2006).

The MD REE belt contains a number of REE deposits or prospects with total REO resources >5Mt (109 Geological Brigade of Sichuan Bureau of Geology and Mineral Resource, 2010), making it one of the most important REE belt/province in the world. Typical REE deposits in the belt include the Maoniuping, Muluozhai, and Lizhuang deposits in the north and Dalucao REE deposit in the south (Fig. 1B). These REE deposits are spatially and genetically related to coeval carbonatite-syenite complexes and tectonically controlled by Cenozoic strike-slip faults (Fig. 1B). Recent geochronological studies have shown that REE deposits in the north were formed at ca. 27 Ma, whereas that in the south

was formed at ca. 12 Ma (Liu et al., 2015; Ling et al., 2016; Liu and Hou, 2017).

2.2. Geology of the Muluozhai REE deposit

2.2.1. Occurrences of ore bodies

The ca. 27 Ma Muluozhai REE deposit is located in the northern part of MD REE belt and tectonically controlled by the Yalongjiang strike-slip fault (Fig. 1B). The deposit contains 0.12 Mt REO resources at an average grade of 3.66 wt% (Liu and Hou, 2017), and is spatially divided into Zhengjialiangzi, Diaoloushan and Fangjiabao sections of which the former two are still active in mining (Fig. 2). In the ore district, the main country rocks are schists, basalts, metadiabase, and Permian marble, all of which are intruded by Cenozoic alkali granite and carbonatite-syenite complex (Fig. 2). The REE ore bodies are mainly hosted in the syenite, metadiabase and marble (Fig. 2). Five ore bodies have been identified in the Diaoloushan district, and have ore grades ranging from 2 to 5 wt%. They are 100 to 400 m in length and 0.5–20 m in thickness. On the other hand, twelve ore bodies with grades less than 5 wt% have been identified in Zhengjialiangzi. They have lengths varying from 40 to 440 m with thicknesses of generally less than 30 m.

2.2.2. Mineralization styles and paragenetic sequence

The deposit is essentially characterized by development of complicated vein systems that are associated with variable alteration on hosting rocks. Fenitization is the earliest alteration and mainly distributed in the Diaoloushan section, followed by carbonatization that is locally present. The fenitization is pervasively overprinting the syenite, and is characterized by the replacement of primary K-feldspar by albite, arfvedsonite, aegirine-augite, and phlogopite. The fenitized syenites is also associated with presences of abundant fenite veins or veinlets that are composed of a broadly similar mineral assemblage including aegirine-augite and subordinate quartz, arfvedsonite, calcite, phlogopite, albite, K-feldspar (Fig. 3A). On the other hand, carbonatization is characterized by a mineral assemblage of calcite, dolomite, barite, celestine, quartz, fluorite, and bastnäsite.

The REE mineralization is essentially characterized by bastnäsite-rich ore veins which generally distributed along tensile fractures and/or lithological contacts. These veins have thicknesses highly variable from several centimeters to several meters, and are suggested to be postdating the fenitization, as they crosscut the finitized syenites (Fig. 4A). It is notable that two generations of ore veins were identified based on mineral assemblages and crosscutting relationships (Fig. 3C-D and 4D). The early generation is widely distributed throughout all the sections and composed mainly of calcite, fluorite, barite and bastnäsite with subordinate quartz, phlogopite, and sulfides (pyrite, galena, and molybdenite, etc.) (Fig. 3C). On the other hand, the late generation, which is only observed in the Diaoloushan section, is distinguishable by containing additionally abundant anhydrite and fluorite (>80 vol%) (Fig. 3D). In addition, we also identified abundant barren veins that clearly predate the two generations of REE mineralizing veins (Fig. 4C) but postdate fenitization (Fig. 4B).

On the basis of macro- and micro-textural relationships among various veins/veinlets (barren of fertile), this study re-established a paragenetic sequence for the Muluozhai deposit, with emphasis on fluorite (Fig. 5). The first stage would be the fenitization stage (Stage I) which is characterized by the formation of the fenitized rocks and associated fenite veins as mentioned above (Fig. 3A). Fluorite in this stage is locally present and occurs as euhedral to subhedral (5–30 mm) grains. This stage is followed by a series of barren veins that are several to tens of meters in widths (Fig. 4B). These veins, named as the pre-REE stage (Stage II), are composed of pegmatitic, coarse-grained fluorite, calcite and barite (Fig. 3B) of which fluorite is the dominant mineral which is generally green in color and occurs as euhedral to subhedral grains or as massive aggregates.

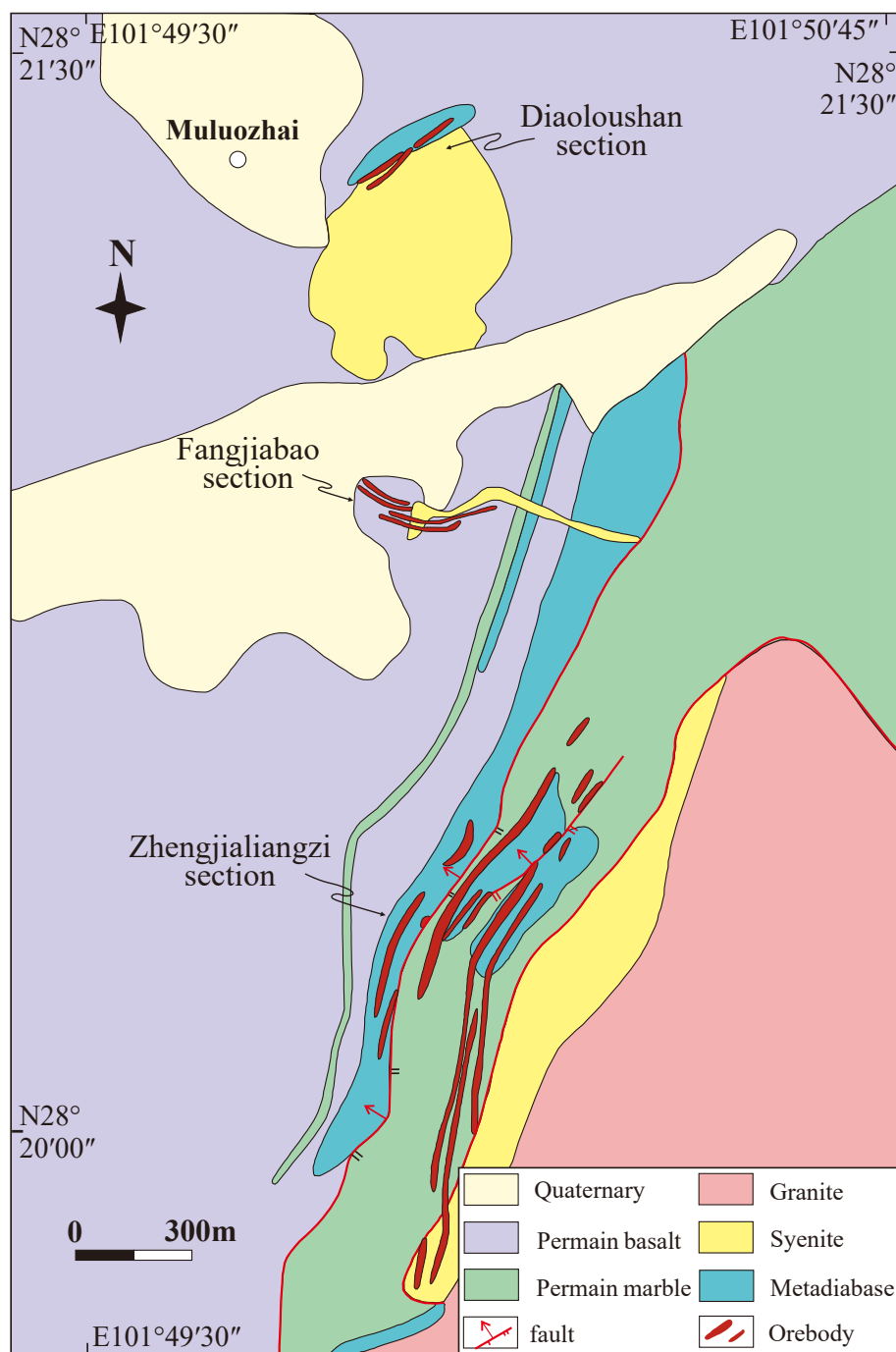Postdating the barren veins of Stage II are the REE-rich ore veins of

Fig. 2. Simplified geological map of the Muluozhai ore district (modified from Liu and Hou, 2017).

two generations (Fig. 4C, D) which were named as Stages III and IV veins, respectively. Fluorite in Stage III veins mainly occurs as euhedral to subhedral crystals with variable diameters from 0.1 to 4 cm. They are purple, green or white in color, and are closely associated with bastnäsite. The late mineralization stage (Stage IV) is distinguishable by presences of abundant anhydrite that is commonly presenting as subhedral to euhedral crystals with diameters up to 2 cm (Fig. 3D). Purple fluorite is subordinate to anhydrite and occurs as fragments of coarse-grained (up to 5 cm) euhedral crystals (Fig. 6H and I) or as small (less than 0.5 cm), cubic grains (Fig. 6F–H).

3. Sampling and analytical methods

3.1. Sampling

Fluorite samples were collected from veins of all the stages. They were examined by scanning electron microscope-cathodoluminescence (SEM-CL), trace elemental, and fluid inclusion analyses. It is notable that before trace elemental and fluid inclusions analyses, detailed SEM-CL imaging was performed to identify internal texture.
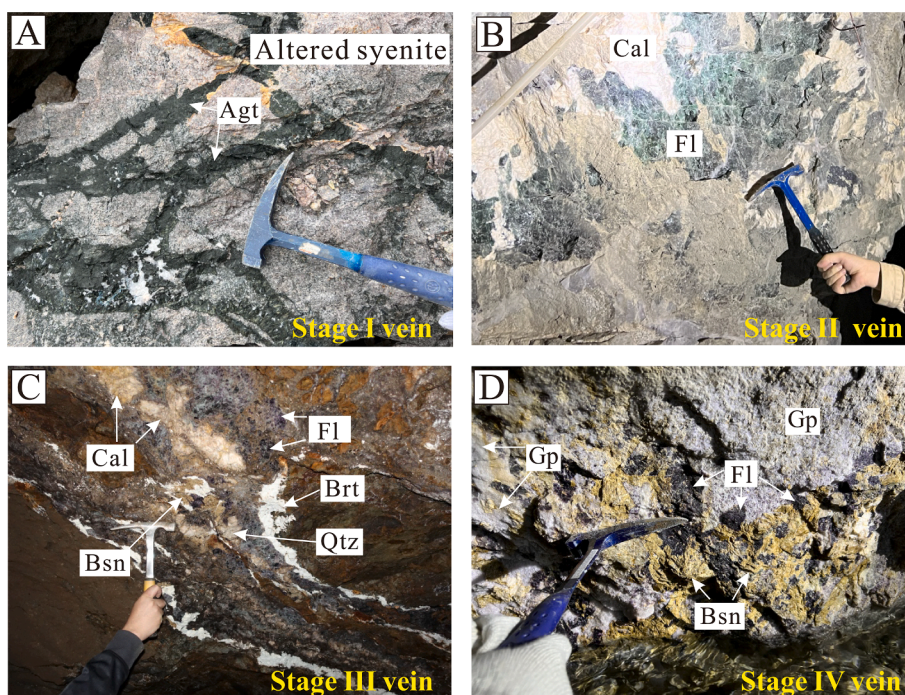
Fig. 3. Field photographs displaying different generations of veins in the Muluozhai deposit. (A) Fenite veins crosscutting syenite; (B) Pegmatitic fluorite-calcite-barite veins composed of coarse-grained calcite, fluorite, barite and quartz; (C) Calcite-quartz-fluorite-barite-bastnäsite veins containing abundant bastnäsite grains; (D) Anhydrite-rich mineralized veins composed of fluorite, anhydrite and bastnäsite.
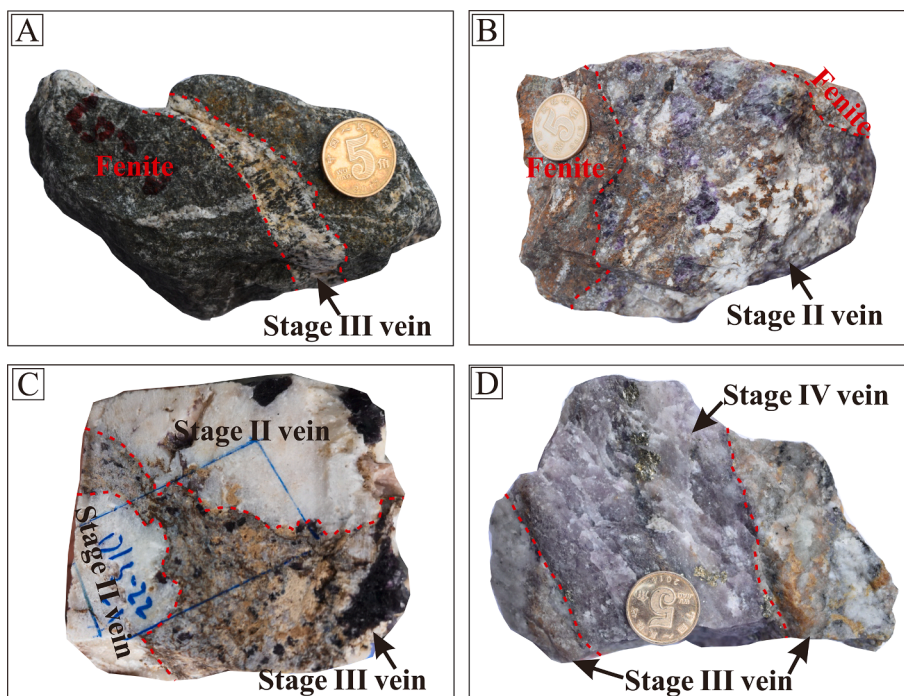
Fig. 4. Representative images of specimens showing crosscutting the relationship of veins in the Muluozhai REE deposit. (A) Calcite vein containing bastnäsite crosscut fenite. (B) Coarse-grained calcite-fluorite-barite vein crosscut fenite. (C) calcite-fluorite-barite-bastnäsite vein crosscut coarse-grained calcite-fluorite vein. (D) Anhydrite-pyrite-fluorite-bastnäsite vein crosscut calcite-fluorite-barite-bastnäsite vein.

3.2. Methods

3.2.1. Scanning electron microscope–cathodoluminescence (SEM-CL) analysis

Detailed SEM-CL imaging of the fluorite and quartz were conducted to distinguish their generations at an accelerating voltage of 15 kV and beam current of ∼ 10nA, using a JSM-7800F thermal field scanning electron microscope (SEM) equipped with a TEAM Apollo XL energy disperse spectroscopy and a Mono CL4 cathodoluminescence spectroscope at the State Key Laboratory of Ore Deposit Geochemistry (SKLODG), Institute of Geochemistry, Chinese Academy of Sciences, Guiyang, China. Polished thin sections were carbon coated before
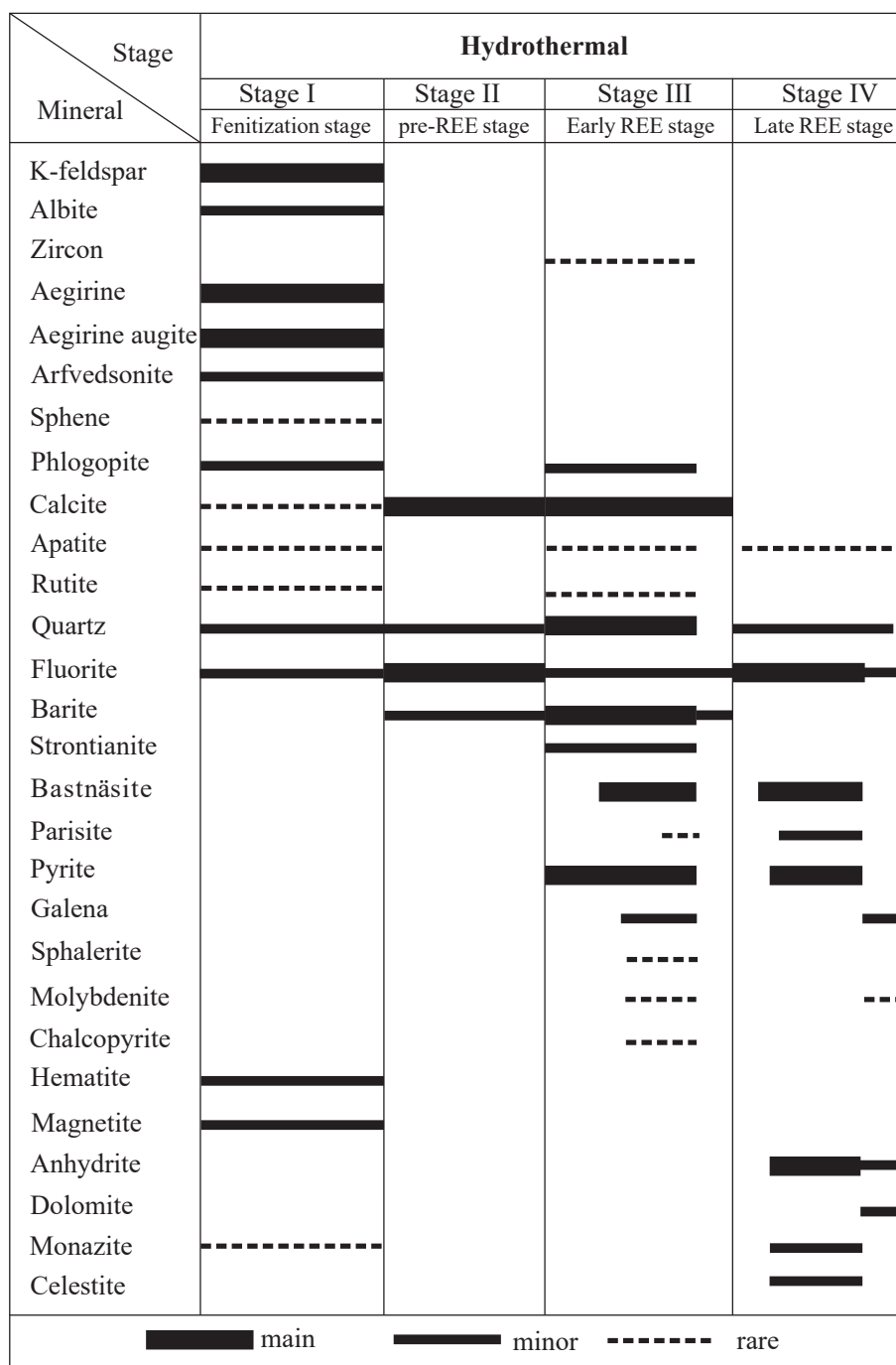
Stage / Mineral	Hydrothermal			
	Stage I	Stage II	Stage III	Stage IV
	Fenitization stage	pre-REE stage	Early REE stage	Late REE stage
K-feldspar	████			
Albite	████			
Zircon			-------	
Aegirine	████			
Aegirine augite	████			
Arfvedsonite	████			
Sphene	-------			
Phlogopite	────		────	
Calcite	-------	████	████	
Apatite	-------		-------	-------
Rutite	-------		-------	
Quartz	────		████	────
Fluorite	────	████		████
Barite		────	████	
Strontianite			────	
Bastnäsite			████	████
Parisite			---	────
Pyrite			████	████
Galena			────	────
Sphalerite			-----	
Molybdenite			-----	---
Chalcopyrite			-----	
Hematite	────			
Magnetite	────			
Anhydrite				████
Dolomite				────
Monazite	-------			████
Celestite				████

████ main ──── minor ------- rare

Fig. 5. Paragenetic sequence of REE and gangue minerals in the Muluozhai deposit.

analysis.

3.2.2. Trace element analyses by LA-ICP-MS

In situ chemical analyses of fluorite were conducted using a Agilent 7900 Quadrupole ICP-MS coupled to a Photon Machines Analyte HE 193-nm ArF Excimer Laser Ablation system equipped with a SQUID signal smoothing device at the In Situ Mineral Geochemistry Lab, Ore and Exploration Centre (ODEC), Hefei University of Technology, Hefei, Anhui Province, China. Helium was used as a carrier gas and was mixed with argon as a makeup gas via a T-connector before entering the torch. The analyses were consistently performed at a laser energy density of 10 J/cm^2, a repetition rate of 10 Hz, and a spot size of 32 μm. Each analysis includes a background acquisition of approximately 20 s for a gas blank, followed by data acquisition of 40 s from the samples. The analyzed trace elements are Li, B, Na, Al, K, Ca, Ti, Mn, Fe, Co, Rb, Sr, Y, Sn, Ba, La, Ce, Pr, Nd, Sm, Eu, Gd, Tb, Dy, Ho, Er, Tm, Yb, Lu, Pb, Th, and U. In order to avoid accident contamination of potential mineral and fluid inclusions, detailed transmitted light and SEM-BSE (CL) images were firstly used for target selecting before ablation. Moreover, signals of some elements such as ^{23}Na, ^{29}Si, ^{39}K, ^{40}Ca and ^{56}Fe were monitored during the analyses to detect possible contamination of mineral and fluid inclusions. The National Institute of Standards and Technology reference (NIST) material SRM 610 and SRM 612 was used as external standards. Each standard sample was measured twice after every 10 analyses of unknown fluorite samples. Off-line data selection and integration were performed by ICPMSDataCal (Liu et al., 2008) using Ca as
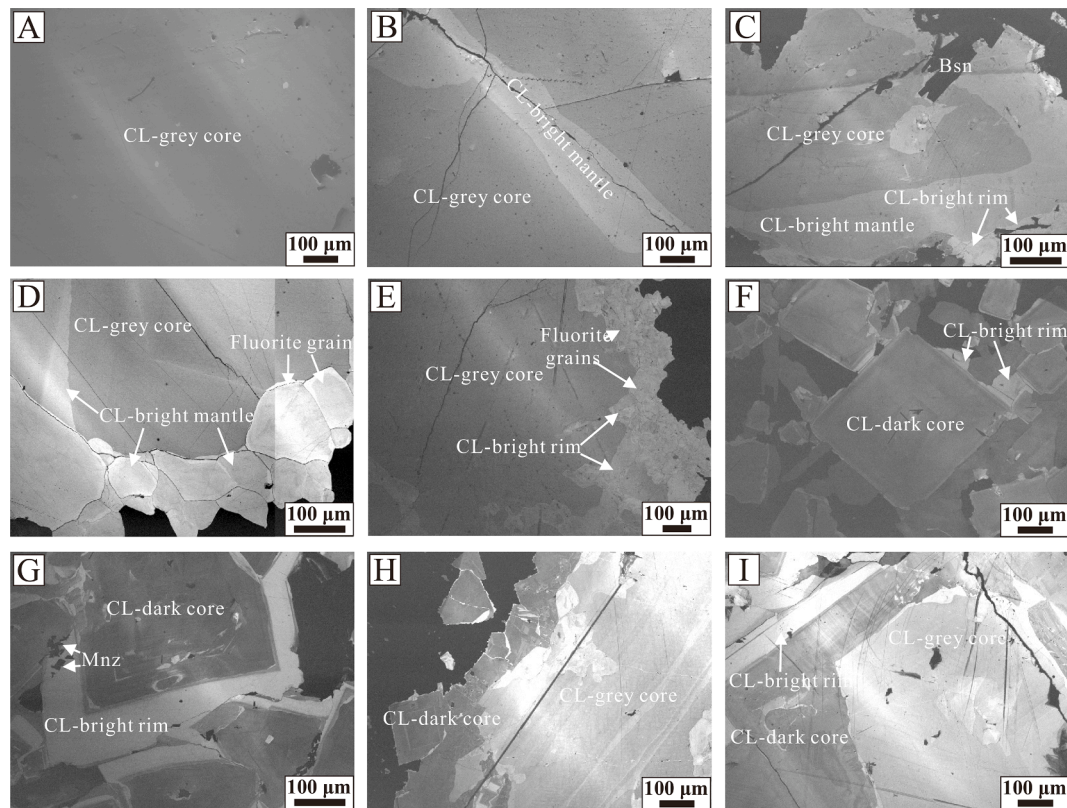
Fig. 6. Cathodoluminescence images showing textures features of fluorite from different stages. (A) Fluorite from Stage I veins with homogeneous texture; (B) Fluorite from Stage II veins showing heterogeneous texture; (C-E) Fluorite from Stage III veins consisting of core, mantle, and rim domains with irregular and sharp contacts; (F-G) Zoned Type II fluorite grains from Stage IV veins with bright rims. Note that the bright rims contain monazite grains; (H-I) Two types of fluorite grains from Stage IV veins. Note that the Type II fluorite is distribute along margin of the Type I fluorite.

the internal standard.

3.2.3. Fluid inclusion microthermometry

Microthermometric measurements of fluid inclusion were undertaken using a Linkham THMSG 600 programmable heating-freezing stage (-196 to + 600 °C) attached to a Leica microscope at the SKLODG. The equipment was calibrated using the synthetic fluid inclusion standard. The accuracy of the temperature measurements is ± 0.1 °C at < 30 °C, and ± 1 °C at > 150 °C. A heating rate of 0.5 °C/min was used to determine melting temperatures of solid CO_2, ice and clathrate, and partial homogenization temperatures of CO_2. The heating rate for measurements of the disappearance temperatures of bubble and solid phase was 2 °C/min. However, not all types of data are available for every inclusion because of the phase-types of the relevant inclusions and difficulties in the observation for some inclusions.

3.2.4. Laser Raman spectroscopy

The Raman spectroscopic analyses of fluid inclusions were carried out at the SKLODG, using a LabRAM HR Evolution with a open space microscope equipped with a 20x objective (NA 0.25) was used to obtain LRS analyses. The laser spot was ~ 2 μm in diameter. A backscattering geometry was used in the 100–4000 cm^{-1} range, using a 600l.mm^{-1} grating. The Raman spectra were acquired by a 532 nm laser, using a power about 25mW, and 2 consecutive acquisitions that lasted 10 s each.

4. Results

4.1. Textures of fluorite from different veins

Fluorite grains are present in all the generations of veins, but exhibit distinctly complex internal textures. Fluorite grains from veins of Stages

I and II are mostly homogeneous under CL imaging (Fig. 6A), with minor displaying inhomogeneous textures similar to those in veins of Stage III (Fig. 6B and C). Indeed, fluorite grains in veins of Stage III exhibit distinct internal textures that generally consist of three domains under CL imaging, named as core, mantle and rim from center outward (Fig. 6C–E). The contacts among these domains are irregular and sharp, and it is common that the rim domains embay both the core and mantle (Fig. 6C and E). The cores are homogeneous, whereas both the mantles and rims are relatively bright and mottled under CL imaging (Fig. 6B–E). It is notable that in the veins of Stage III, there are also minor individual fluorite grains that are homogeneous and present as euhedral to subhedral habits (Fig. 6D–E).

In the veins of Stage IV, two types of fluorites can be texturally identified. Type I ones are presenting as brecciated grains that display complex internal textures comparable to those in Stage III veins (Fig. 6H–I). In contrast, Type II ones are cubic in shapes, and consist of CL-dark cores and CL-bright rims with regular contacts (Fig. 6F–I). Type I ones should predate Type II ones, as they are overgrown or replaced by Type II fluorite along margins (Fig. 6H and I).

4.2. Chemical composition of fluorite

Trace element compositions of all the domains in fluorite from veins of different stages were analyzed by LA-ICP-MS. The main trace elements in the fluorite are Na, Si, Fe, and Sr, while others such as Cr, Mg, Ga, and Mn are minor or below detection limit (Appendix Table 1; Fig. 7). The results show that the corresponding domains (e.g., the cores, mantles or rims) for fluorite of Stages I to III veins and Type I fluorite of Stage IV veins have comparable compositions (Appendix Table 1; Figs. 7 and 9). Generally, cores have highest Na (63–333 ppm) and Ga (0.56–3.72 ppm), and have Mg, Mn, and Sr contents similar to the
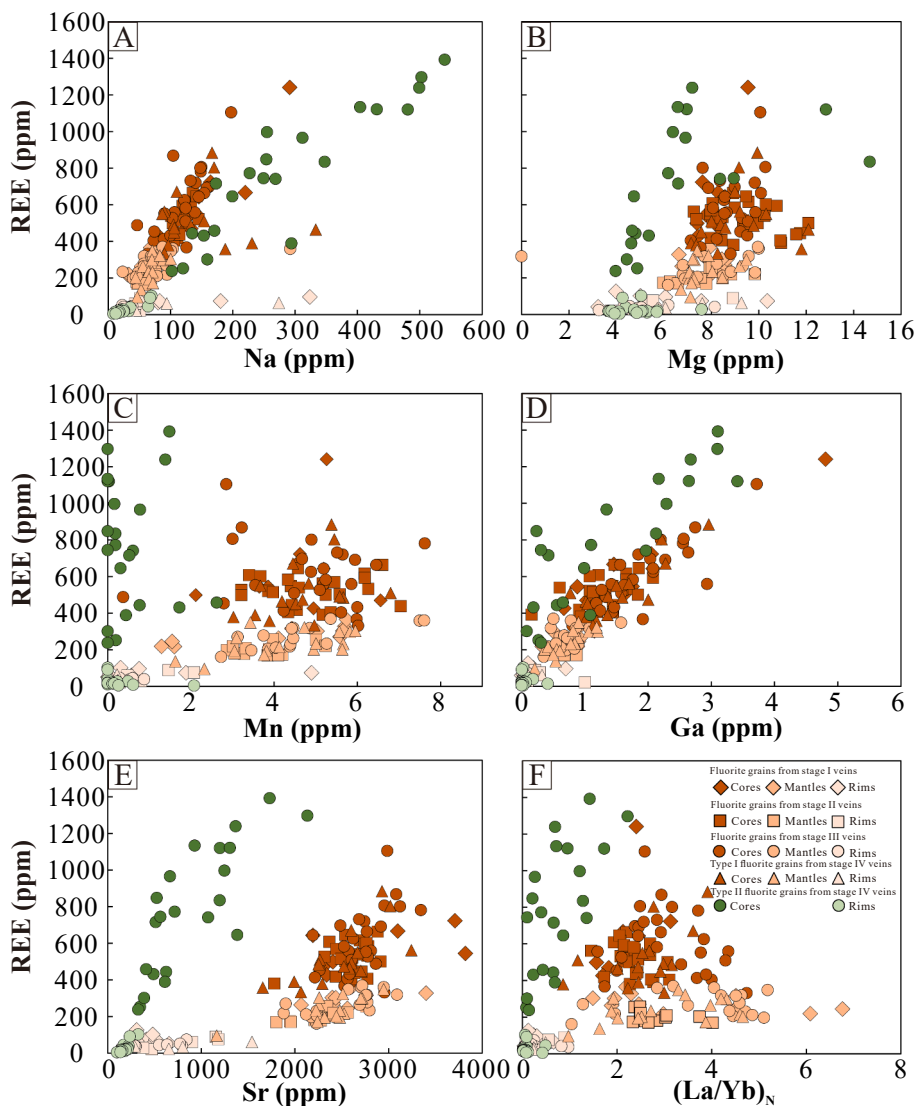
Fig. 7. Bimodal plots of REE vs. Na (A), REE vs. Mg (B), REE vs. Mn (C), REE vs. Ga (D), REE vs. Sr (E), and REE vs. (La/Yb)$_N$ (F) for different domains in the fluorite. Chondrite values are from McDonough and Sun (1995).
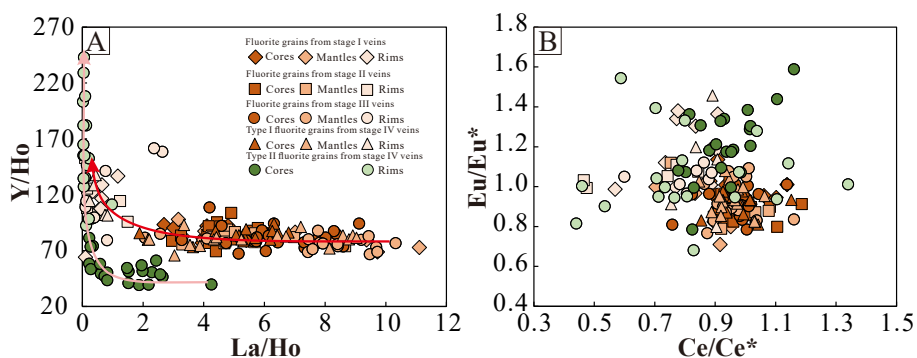

Fig. 8. Bimodal plots of Y/Ho vs. La/Ho (A), and Eu/Eu* vs. Ce/Ce* (B) for different domains in the fluorite. Chondrite values are from McDonough and Sun (1995).

mantles but higher than rims (Fig. 7). On the other hand, the cores of Type II fluorite in Stage IV veins have Na (102–540 ppm) higher but Mn (0–2.26 ppm), and Sr (327–2134 ppm) contents lower than Type I fluorite (Fig. 7). However, rims of both types have similarly low Na, Mg, Mn, and Sr contents (Fig. 7).

Similar to the trace elements mentioned above, the corresponding

domains for fluorite of Stages I to III veins and Type I fluorite of Stage IV veins have also comparable REE contents, and exhibit similar chondrite-normalized REE patterns (Figs. 7 and 8). For example, the cores of these grains have total REE contents similarly higher than the mantles, but both the cores and mantles show parallel, relatively flat REE patterns on the chondrite-normalized REE diagrams (Fig. 9). In contrast, the rim
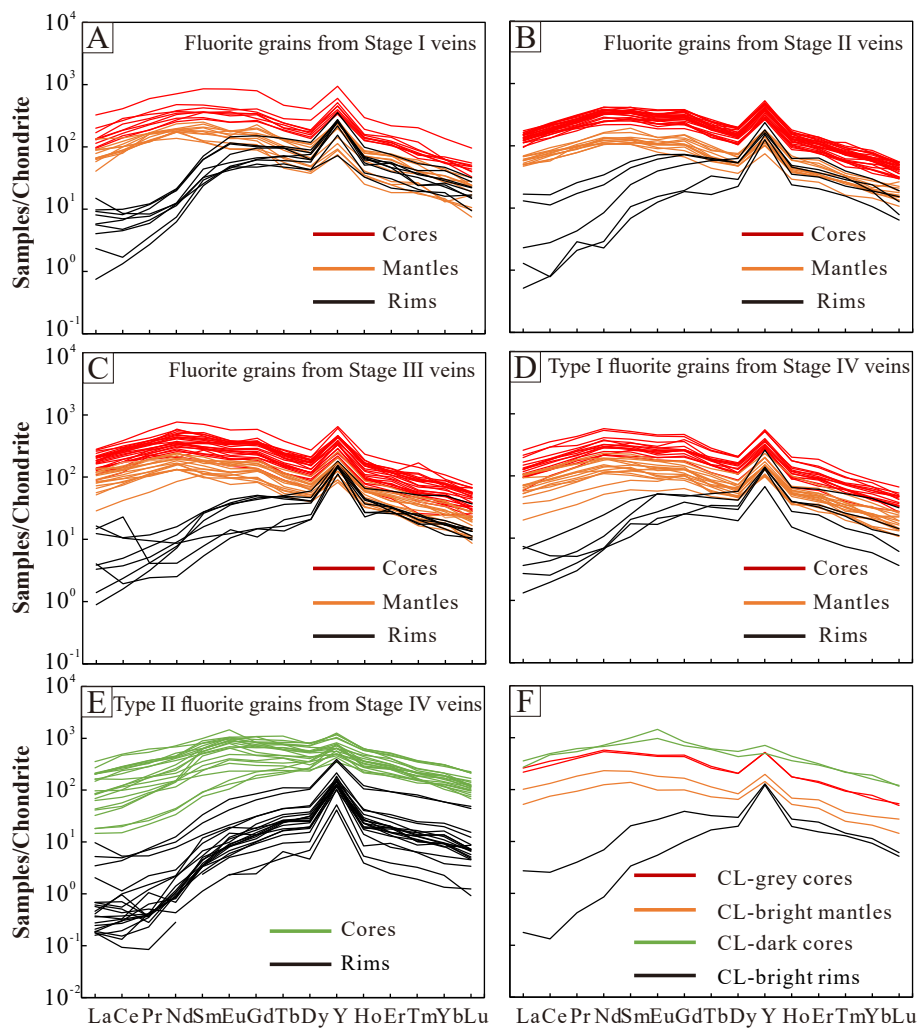
Fig. 9. Chondrite-normalized REE patterns of different domains in the fluorite from Stages I to III veins (A-C); Type I (D) and Type II fluorite (E) from Stage IV veins; An individual fluorite grains containing Type I and II fluorite from Stage IV veins (such as Fig. 6H and I) (F). Chondrite values are from McDonough and Sun (1995).
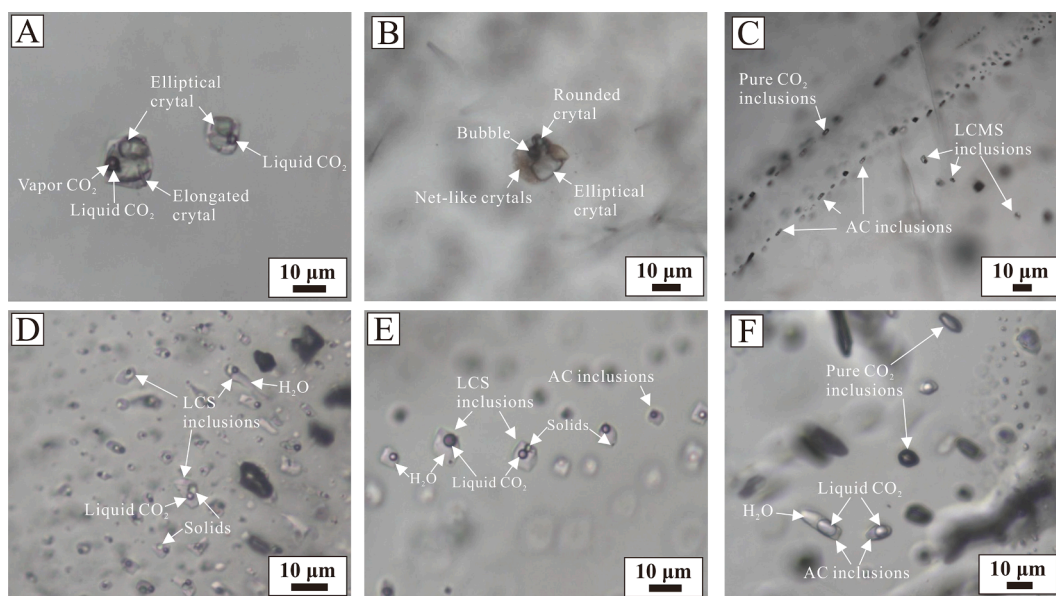
Fig. 10. Photomicrographs of different types of fluid inclusions in the Muluozhai deposit. (A-B) LCMS inclusions comprising multi-solids; (C) Coexistence of LCMS inclusions and secondary AC inclusions; (D) Cluster of LCS inclusions; (E) Coexistence of AC inclusions and LCS inclusions; (F) Coexistence of AC inclusion and C inclusions in fluorite of stage IV veins.

domains exhibit remarkably low REE contents and distinctly LREE-depleted, inverted U-shape REE patterns (Fig. 9). As such, both the core and mantle domains have similarly high $(La/Yb)_N$ and Ce/Ce* ratios but low Y/Y* and Eu/Eu* ratios relative to the rim domains (Fig. 8). For Type II fluorite from Stage IV veins, the CL-dark cores exhibit flat chondrite-normalized REE patterns that are broadly similar to cores of fluorite in Stages I to III, but display relatively inconspicuous Y anomaly (Fig. 9E and F). In contrast, the CL-bright rims of this type have much lower REE contents and display LREE-depleted chondrite-normalized REE patterns (Fig. 9E).

4.3. Fluid inclusion petrography

Fluid inclusions were observed in fluorite from Stages I to IV veins. Based on the petrographic features (e.g., phase and phase ratios) at room temperature, these fluid inclusions were grouped into four types (Fig. 10) including (1) liquid-carbonic inclusions containing three or more solids (LCMS); (2) liquid-carbonic inclusions containing one or two solids (LCS); (3) pure CO_2 inclusions (C); and (4) aqueous-carbonic inclusions (AC).

The same type of fluid inclusions from different stages of veins has similar petrographic features. The LCMS inclusions show rounded, elliptical, and irregular shapes with diameters varying from 5 to 150 μm (Fig. 10A–C). They generally consist of several solids, liquid CO_2, vapor CO_2, and minor liquid phases (Fig. 10A–C). The solid phases occupy >70 vol% of the inclusion, and exhibit rounded, elliptical, elongated, cubic, rounded and net-like shapes (Fig. 10A–C). The LCS inclusions are irregular or rounded in shapes and 5 to 25 μm in size (Fig. 10D–E). The LCS inclusions are distinguishable from LCMS inclusions by notably smaller solid crystals with a significantly higher percentage of aqueous phase (>50 vol%, Fig. 10A–E). They consisted of one to two solid crystals, aqueous and vapor phase. The solid crystals in LCS inclusions are generally elongated, elliptical, and rounded in shapes and occupy less than 20 vol% of the inclusions. They commonly occur as clusters in fluorite. AC inclusions are generally negative-crystal, elliptical, rounded, and irregular shapes with diameters varying from 5 to 50 μm (Fig. 10F). This type of inclusions commonly occurs as clusters and in some cases as secondary trails in fluorite. These inclusions commonly comprise aqueous and liquid CO_2 at room temperature, and vapor CO_2 appears during cooling. Rarely, three phases are present (e.g., aqueous + liquid CO_2 + vapor CO_2) at room temperature. The CO_2 bubble occupies 10–70% of the total volume. Pure CO_2 inclusions comprise only a carbonic phase and are elliptical and negative-crystal in shapes with diameters ranging from 5 to 40 μm. The pure CO_2 inclusions usually coexist with the aqueous-carbonic inclusions.

All types of fluid inclusions can be identified in fluorite from Stages I to III veins and Type I fluorite in Stage IV veins, while only LCMS inclusions are observed in cores of Type II fluorite. No inclusions were identified in rims of Type II fluorite, possibly due to the shallow feature of the rims. Generally, the distribution of different types of fluid inclusion is well correlated with textures of fluorite in multi-generation veins. For example, the LCMS inclusions occur in the core domains, LCS inclusions occur in the mantle domains, and AC inclusions occur in both the mantle and rim domains of fluorite grains. Types of inclusions present in the cores, mantles and rims of the Type I fluorite grains in Stage IV veins are broadly similar to those of fluorite in Stage III veins. It is notable that the coexistence of LCS and AC inclusions, which records fluid immiscibility (Fig. 10E), is common in the mantle domains of Type I fluorite from Stage IV veins.

4.4. Microthermometry

The detailed microthermometric data of all types of inclusions are provided in Appendix Table 2 and summarized in Table 1. The LCMS, LCS and some AC inclusions are rich in sulfate (see below), and thus salinities of these inclusions currently cannot be obtained through microthermometric analyses.

The LCMS inclusions hosted in core domains of fluorite grains from different stages of veins were all homogenized by the disappearance of vapor phase after dissolution of solids. These inclusions hosted in core domains of fluorite in Stages I to III veins have the solids dissolution temperatures varying from 489 to > 600 °C, 526 to > 600 °C, and from 456 to > 600 °C, respectively (Fig. 11). The LCMS inclusions hosted in core domains of the Type I and II fluorite from Stage IV veins have similar solid dissolution temperatures ranging from 532 to > 600 °C and from 512 to > 600 °C (Fig. 11). In most cases, a small bubble still exists in the inclusions at temperatures of 600 °C, which is the maximum temperature achievable with the current apparatus. This suggests that these inclusions have high homogenization temperature of >600 °C.

In most cases, the LCS inclusions were generally homogenized by the disappearance of bubble after dissolution of solids, but in rare cases they were homogenized by dissolution of solids after disappearance of vapor phase (Appendix Table 2), indicating that the solids are captured phase. The LCS inclusions hosted in mantle domains of fluorite in Stages II to IV veins have similar solid dissolution and final homogenization temperatures (Fig. 11). The solid dissolution occurred at 159 to 240 °C, 149 to 230 °C and 147 to 259 °C, while the final homogenization temperatures vary from 312 to 392 °C, 305 to 373 °C and 316 to 405 °C, respectively (Fig. 11). The secondary LCS inclusions identified in core domains of fluorite in Stage I veins have solid dissolution and final homogenization temperatures broadly similar to those of LCS inclusions identified in core domains of fluorite from Stages II to IV veins, varying from 164 to 430 °C and 307 to 430 °C, respectively (Fig. 11).

All the AC inclusions formed solid CO_2 when the temperature

Table 1
Microthermometric results of fluid inclusions in the Muluozhai deposit.

Stage	inclusion type	Bubble volume (%)	Tm-CO₂ (°C)	Tm-ice (°C)	Tm-cla (°C)	Th-CO₂ (°C)	Th-solid (°C)	Th-(L-V) (°C)
Stage I	LCMS	< 10					489 to > 600	587 to > 600
	LCS	< 20					164 to 430	307 to 430
	AC	40 to 60	−57.4 to −56.3		6.4 to 7.6	6.9 to 8.5		224 to 293
Stage II	LCMS	< 10					526 to > 600	>600
	LCS	20 to 30					159 to 240	312 to 392
	AC	20 to 60	−56.5 to −55.7	−1.8 to −1.4	6.2 to 9.2	6.5 to 10.3		173 to 311
Stage III	LCMS	< 10					456 to > 600	587 to > 600
	LCS	15 to 30					149 to 230	305 to 373
	AC	10 to 70	−57.2 to −55.7	−2.5 to −1.5	5.3 to 9.3	5.9 to 24.1		156 to 310
Stage IV	LCMS (Type I fluorite)	< 10					532 to > 600	>600
	LCMS (Type II fluorite)	< 10					512 to > 600	582 to > 600
	LCS	10 to 40					147 to 259	316 to 405
	AC (Mantle)	40			7.8 to 7.9	5.7 to 5.9		367 to 387
	AC (Rim)	20 to 70	−58.0 to −55.6	−2.6 to −1.8	6.8 to 9.1	0.7 to 7.3		169 to 320

Notes: Tm-CO₂ = Solid CO₂ melting temperature, Tm-ice = ice melting temperature, Tm-cla = clathrate melting temperature, Th-CO₂ = partial homogenization temperature of CO₂ phase, Th-solid = solid dissolution temperature, Th-(L-V) = liquid (L) or vapor (V) disappearance temperature.
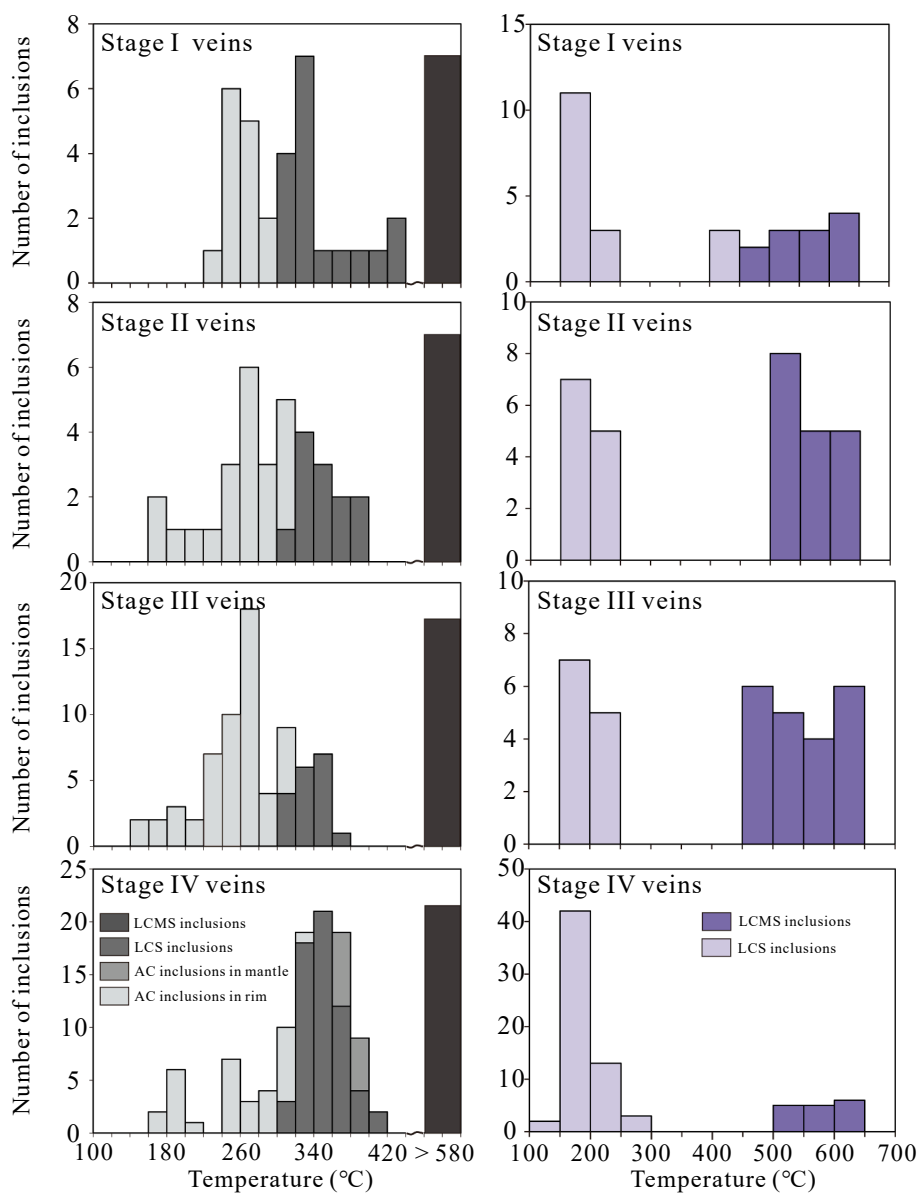
Fig. 11. Histograms showing the microthermometric results of different types of fluid inclusions in the Muluozhai deposit. Histograms on the left display final homogenization temperatures of inclusions in fluorite from the Stages I to IV veins. Histograms on the right show the temperatures of solid phases dissolution in LCMS and LCS inclusions in fluorite from Stages I to IV veins.

dropped to − 100 °C. The solid CO_2 decomposed at temperatures of about −56 °C. AC inclusions in rim domains of fluorite in Stages I to IV veins have clathrate decomposing at temperatures of 6.4 to 7.6 °C, 6.2 to 9.2 °C, 5.3 to 9.3 °C, and 6.8 to 9.1 °C, respectively. Most AC inclusions have a critical homogenization behavior. These inclusions hosted in rim domains of fluorite in Stages I to IV veins have similar final homogenization temperatures varying from 224 to 293 °C, 173 to 311 °C, 156 to 310 °C, 169 to 320 °C, respectively. However, AC inclusions in the immiscible assemblages in fluorite of the Stage IV veins have remarkably higher final homogenization temperatures (367 to 387 °C, Appendix Table 2).

4.5. Raman spectroscopic analysis

Raman spectroscopic analyses were conducted on the bubble, aqueous and solid phases in the fluid inclusions. Selections of spectrograms are presented in Fig. 12.

In all types of inclusions, peaks at 1279 cm^{-1} and 1384 cm^{-1} are

observed in the bubble, suggesting the presence of CO_2 (Fig. 12). The liquid phases in the LCMS, LCS and AC inclusions (coexisting with LCS inclusions) have strong Raman peaks at 981 to 984 cm^{-1} and around 3500 cm^{-1}, indicating that H_2O dominates the aqueous phases in which SO_4^{2-} is the major anion (Fig. 12).

The Raman peaks of solid phases in LCMS inclusions hosted in core domains of fluorite in different-stage veins are similar and occur frequently at 987, 993, 996, 999 and 1004 cm^{-1} (Fig. 12), suggesting that the solid phases were dominated by sulfate (e.g., aphthitalite, barite, thenardite, celestite, and leightonite). Subordinate Raman peaks are 451, 621, 1004, and 1045 cm^{-1}, corresponding to blodite, burkeite, gypsum, and nahcolite, respectively. Other Raman peaks include 1084 and 1095 cm^{-1}, indicative of calcite and dolomite, respectively. For solid phases in LCS inclusions, only Raman peaks of barite, thenardite, and nahcolite have been identified (Fig. 12).
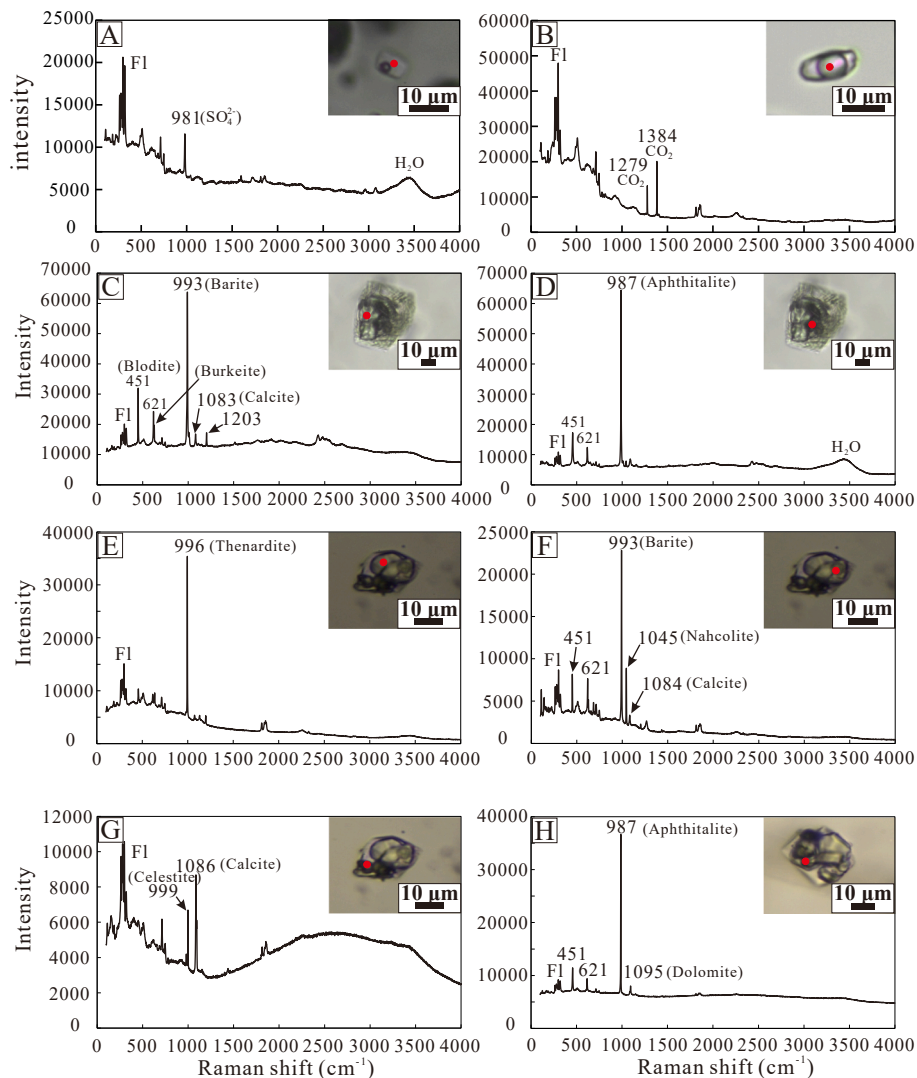
Fig. 12. Laser Raman spectra of fluid inclusions in the fluorite from the Muluozhai deposit. (A) SO_4^{2-} and H_2O in aqueous phase of AC inclusion; (B) CO_2 in bubble phase of AC inclusion; (C-H) Laser Raman spectra of solid in LCMS inclusions. Note that solids include blodite, burkeite, barite, calcite (C), aphthitalite (D), thenardite (E), blodite, burkeite, barite, nahcolite, calcite (F), celestite, calcite (G), aphthitalite, and dolomite (H).

5. Discussion

5.1. Comparison and origin of various domains in fluorite from multiple-stage veins

5.1.1. Grain-scale variations

Our results show that fluorite grains from Stages I to III veins and Type I fluorite grains in Stage IV veins exhibit similarly core-mantle-rim internal textures (Fig. 6). LA-ICP-MS trace elemental analyses demonstrate that these domains in an individual fluorite grain show significant variations in REE contents and/or patterns with the cores having highest REE contents and relatively flat REE patterns (Figs. 7–9). The preservation of original shape of the crystals and presences of micro-porosities in the mantle and rim domains (Fig. 6C and E) suggest that such kind of complicate fluorite grains have formed from interaction of the precursors (i.e., cores) with multi-stage fluids via a coupled dissolution-reprecipitation process (Putnis, 2002, 2009). On the other hand, the Type II fluorite grains from late REE veins (i.e., Stage IV) are also generally euhedral and exhibit regular or even slightly oscillatory zonation (Fig. 6F–I). This feature indicates that Type II fluorite grains have normally precipitated from Stage IV fluids without any overprints of late hydrothermal events (Schönenberger et al., 2008; Assadzadeh

et al., 2017).

5.1.2. Correlation of various domains in fluorite with multiple stages

The presences of multiple domains in fluorite of single-stage veins from Stage I to IV (Fig. 6) strongly suggest that they have formed from complex, multi-pulse fluid overprint events (Assadzadeh et al., 2017). In order to precisely constrain the origin of various domains and related causative fluids, a comprehensive comparison of various domains in fluorite from veins of different stages, in terms of chemical compositions and fluid inclusions, was made. The trace elemental results show that the cores of fluorite grains in veins of different stages have similar chemical compositions (Figs. 7 and 8). This is well reflected by their comparable REE contents and chondrite-normalized REE patterns (Fig. 9). The similarity is also available for the mantles or rims of the fluorite grains in multi-generation veins. Such chemical similarities do not support a straightforward explanation that the core-mantle-rim fluorite present in each stage of veins has evolved from a pulse of fluid. The reason is that the nature of different-stage fluids is dramatically different (e.g., REE-rich or REE-barren), and thus cannot precipitate fluorite grains with undistinguishable chemical compositions. Instead, we propose that the cores (or mantles or rims) from these veins are products of a common-stage fluid, and original ones of them were

"captured" by late-stage fluids. This interpretation is further supported by the thermometric results of fluid inclusions. For example, the LCMS inclusions hosted in cores and LCS inclusions hosted in mantles of fluorite in Stages I to III veins have similarly high homogenization temperatures (456 to > 600 °C and 307 to 403 °C, respectively) and comparable daughter crystals (e.g., aphthitalite, barite, thenardite, celestite, and leightonite) (Figs. 11 and 12). It is thus concluded that the core and mantle domains of fluorite in different-generation veins are essentially the crystals forming in Stages I and II, respectively. On the other hand, the AC inclusions hosted in the rims of fluorite in these veins have decreasing homogenization temperatures varying from 330 to 150 °C (Table 1; Fig. 11), correlated well with previous obtained homogenization temperatures for bastnäsite (Zheng et al., 2019). This feature indicates that formation of the rims is genetically related to the fluids of Stage III.

In the veins of Stage IV, the Type I fluorite grains exhibit similar core-mantle-rim texture, and have chemical compositions and thermometric features of fluid inclusions of each domain comparable to those of Stages I to III veins (Figs. 7 and 11), thus indicative of a similar origin of these grains to those in veins of Stages I to III. In other words, the Type I grains are essentially "xenocrysts" captured by the Stage IV fluids that precipitated the Type II fluorite grains.

5.2. Fluorite as a vector to REE mineralization

This study convincingly confirmed that the cores, mantles and rims of fluorite in various veins are essentially formed from fluids of Stages I, II and III, respectively, whereas the Type II fluorite in Stage IV veins are products of Stage IV fluids. Such a new finding thus allows us to precisely and reliably decipher fluid evolution and origin of the Muluozhai deposit. The cores, mantles and rims exhibit comparable Y/Ho ratios with a narrow range (Fig. 8A). This feature, in combination with the decreasing homogenization temperatures, suggests that Stages I to III were formed from a common fluid related to the causative carbonatite (Bau and Dulski, 1995). Compared to the cores, the mantles exhibit parallel chondrite-normalized patterns (Fig. 9), consistent with the fact that REE minerals not deposited from fluids at Stage II. However, the drop of total REE contents tends to indicate incursion of a small portion of external, REE-poor fluid which only diluted the REE content of the evolved Stage I fluids. The potential candidate for the external fluids could be likely REE-depleted meteoric water (Samson and wood, 2005; Assadzadeh et al., 2017) as also previously documented (Zheng et al., 2019). Considering that the introduction of meteoric water is able to buffer acidic fluids to high pH, a condition favored by precipitation of bastnäsite (Migdisov and Williams-Jones, 2014), we further proposed that the significant drop of REE contents (particular LREE) in the rims (i. e., Stage III) indicate more incursion of the meteoric water which would trigger REE deposition as bastnäsite in Stage III (Fig. 6C).

The Type II fluorite grains, which represent the products precipitated from Stage IV fluids, exhibits highly variable trace elemental contents and chondrite-normalized REE patterns that are distinct from those of Stages I to III (Figs. 7–9). Moreover, the fluid inclusions in the grains have much higher homogenization temperatures (512 to > 600 °C). All these features indicate involvement of a new pulse of relatively high-T REE-rich fluids for the REE mineralization of Stage IV, which is further supported by the different Y/Ho-La/Ho variation trend of fluorite (Fig. 8A). We speculate that this pulse of fluids could represent a new exsolution of REE-rich fluid from carbonatitic melts underneath. The decreasing of LREE contents and $(La/Yb)_N$ values from cores outward of the Type II fluorite could be simply explained by precipitation of REE minerals from the newly exsolved REE-rich fluid.

5.3. General implications

This study confirmed that different generations of fluorites could be present in veins of a specific stage. Such a phenomenon regarding

presences of early-stage "xenocrysts" in late-generation veins should be more common in carbonatite-related vein systems than previously thought, which possibly could be used to explain highly variable chemical compositions or recorded temperatures (through fluid inclusions) for specific minerals in single-stage veins (e.g., Liu et al., 2019; Zheng et al., 2019). As such, detailed investigations in textural context should be prerequisite before using them to interpret fluid evolution or origin of ore deposits.

Our works also show that fluorite is indeed sensitive to physico-chemical conditions of fluids, and thus could be a promising indicator mineral for fluid evolution of a specific carbonatite-related deposit. For example, our new results reveal that the formation of the Muluozhai deposit has likely involved two pulses of REE-rich fluids exsolved from carbonatitic melts. Considering that similar development of complex vein systems is common in other well-known carbonatite-related deposits (such as the Maoniuping and Weishan REE deposits in China), we speculate that such a phenomenon regarding multi-stage contributions of REE-rich fluids from causative carbonatites would be widespread in such kind of deposits.

6. Conclusion

This study provides a good example for using combined textural, in-situ trace elemental and fluid inclusion analyses of fluorite to constrain the nature and evolution of ore-forming fluids in carbonatite-related REE vein systems. It is convincingly confirmed that the core, mantle and rim domains of fluorite in veins of different generations are essentially formed from fluids of Stages I, II and III, respectively. In other words, early formed minerals that are supposed to be present in early-generation veins was easily "captured" by late fluids and thus present as "xenocrysts" in late-generation veins. This new finding may provide a potentially good explanation for many deposits which exhibit highly variable chemical or thermometric data for veins of only a specific stage. On the basis of the new findings above, this study further constrains that the formation of the Muluozhai deposit have likely involved two pulses of carbonatite-expelled REE-rich fluids which are responsible for the two stages of REE mineralization. Such a model involving multiple pulses of fluids may be also applicable for other carbonatite-related REE deposits which particularly develop similar vein systems.

Declaration of Competing Interest

The authors declare that they have no known competing financial interests or personal relationships that could have appeared to influence the work reported in this paper.

Data availability

The data that has been used is confidential.

Appendix A. Supplementary data

Supplementary data to this article can be found online at https://doi.org/10.1016/j.oregeorev.2023.105546.

References

Assadzadeh, G.E., Samson, I.M., Gagnon, J.E., 2017. The trace element chemistry and cathodoluminescence characteristics of fluorite in the Mount Pleasant Sn-W-Mo deposits: Insights into fluid character and implications for exploration. J. Geochem. Explor. 172, 1–19.

Bau, M., Dulski, P., 1995. Comparative study of yttrium and rare-earth element behaviors in fluorine-rich hydrothermal fluids. Contrib. Mineral. Petrol. 119, 213–223.

Bau, M., Romer, R.L., Lüders, V., Dulski, P., 2003. Tracing element sources of hydrothermal mineral deposits: REE and Y distribution and Sr-Nd-Pb isotopes in fluorite from MVT deposits in the Pennine Orefield. England. Miner. Deposita 38 (8), 992–1008.

Beland, C.M.J., Williams-Jones, A.E., 2021. The genesis of the Ashram REE deposit, Quebec: insights from bulk-rock geochemistry, apatite-monazite-bastnäsite replacement interactionions and mineral chemistry. Chem. Geol. 278, 12098.

Geological Brigade of Sichuan Bureau of Geology and Mineral Resource, 2010. Exploration report of Maoniuping REE deposit in Mianning, Sichuan Province.

Broom-Fendley, S., Brady, A.E., Wall, F., Gunn, G., Dawes, W., 2017. REE minerals at the Songwe Hill carbonatite, Malawi: HREEenrichment in late-stage apatite. Ore Geol. Rev. 81, 23–41.

Castor, S.B., 2008. The Mountian Pass rare-earth carbonatite and associated ultrapotassic rocks, California. Can. Mineral. 46, 779–806.

Cheng, Z.G., Zhang, Z., Aibai, A., Kong, W., Holtz, F., 2018. The role of magmatic and postmagmatic hydrothermal processes on rare-earth element mineralization: A study of the Bachu carbonatites from the Tarim Large Igneous Province, NW China. Lithos 314–315, 71–87.

Cong, B.L., 1988, Formation and Evolution of the Panxi Paleo-Rift. Science Press, Beijing, p. 427 (in Chinese).

Deng, X.H., Chen, Y.J., Yao, J.M., Bagas, L., Tang, H.S., 2014. Fluorite REE-Y (REY) geochemistry of the ca. 850 Ma Tumen molybdenite–fluorite deposit, eastern Qinling, China: constraints on ore genesis. Ore Geol. Rev. 63, 532–543.

Duan, Z.P., Jiang, S.Y., Su, H.M., Zhu, X.Y., Jiang, B.B., 2022. Textural features and in situ trace element analysis of fluorite from the Wujianfang fluorite deposit, Inner Mongolia (NE China): insights into fluid metasomatism and ore-forming process. Ore Geol. Rev. 147 (104982), 1–15.

Gagnon, J.E., Samson, I.M., Fryer, B.J., Williams-Jones, A.E., 2003. Compositional heterogeneity in fluorite and the genesis of fluorite deposits: insights from LA-ICPMS analysis. Can. Mineral. 41 (2), 365–382.

Guo, Z., Hertogen, J., Liu, J., Pasteels, P., Boven, A., Punzalan, L., He, H., Luo, X., Zhang, W., 2005. Potassic magmatism in western Sichuan and Yunnan provinces, SE Tibet, China: petrological and geochemical constraints on petrogenesis. J Petrol 46, 33–78.

Gysi, A.P., Williams-Jones, A.E., 2015. The thermodynamic properties of bastnäsite-(Ce) and parisite-(Ce). Chem. Geol. 392, 87–101.

Hill, G.T., Campbell, A.R., Kyle, P.R., 2000. Geochemistry of southwestern New Mexico fluorite occurrences implications for precious metals exploration in fluorite-bearing systems. J. Geochem. Explor. 68 (1-2), 1–20.

Hou, Z., Cook, N.J., 2009. Metallogenesis of the Tibetan collisional orogen: a review and introduction to the special issue. Ore Geol. Rev. 36 (1-3), 2–24.

Hou, Z., Tian, S., Yuan, Z., Xie, Y., Yin, S., Yi, L., Fei, H., Yang, Z., 2006. The Himalayan collision zone carbonatites in western Sichuan, SW China: Petrogenesis, mantle source and tectonic implication. Earth Planet Sc Lett 244 (1–2), 234–250.

Jia, Y.H., Liu, Y., 2020. REE Enrichment during Magmatic-Hydrothermal Processes in Carbonatite-Related REE Deposits: a Case Study of the Weishan REE Deposit. China. Minerals 10, 25.

Ling, X.X., Li, Q.L., Liu, Y., Yang, Y.H., Liu, Y., Tang, G.Q., Li, X.H., 2016. In situ SIMS Th–Pb dating of bastnaesite: constraint on the mineralization time of the Himalayan Mianning–Dechang rare earth element deposits. J. Anal. Atom. Spec. 31 (8), 1680–1687.

Liu, Y., Hou, Z.Q., 2017. A synthesis of mineralization styles with an integrated genetic model of carbonatite-syenite-hosted REE deposits in the Cenozoic Mianning–Dechang REE metallogenic belt, the eastern Tibetan Plateau, southwestern China. J. Asian Earth Sci. 137, 35–79.

Liu, Y., Hou, Z.Q., Tian, S.H., Zhang, Q.C., Zhu, Z.M., Liu, J.H., 2015. Zircon U-Pb ages of the Mianning–Dechang syenites, Sichuan Province, southwestern China: constraints on the giant REE mineralization belt and its regional geological setting. Ore Geol. Rev. 64, 554–568.

Liu, Y., Chakhmouradian, A.R., Hou, Z., Song, W., Kynický, J., 2019. Development of REE mineralization in the giant Maoniuping deposit (Sichuan, China): insights from mineralogy, fluid inclusions, and trace-element geochemistry. Mineral. Deposita 54 (5), 701–718.

Liu, Y.S., Hu, Z.C., Gao, S., Günther, D., Xu, J., Gao, C.G., Chen, H.H., 2008. In situ analysis of major and trace elements of anhydrous minerals by LA-ICP-MS without applying an internal standard. Chem. Geol. 257 (1–2), 34–43.

Luo, Y.N., Yu, R.L., Hou, L.W., Lai, S.M., Fu, D.M., Chen, M.X., Fu, X.F., Rao, R.B., Zhou, S.S., 1998. Longmenshan-Jinpingshan Intracontinental Orogenic Belt. In: Sichuan Science and Technology Publishing House, p. 171 in Chinese.

McDonough, W.F., Sun, S.-s., 1995. The composition of the Earth. Chem. Geol. 120 (3-4), 223–253.

Migdisov, A.A., Williams-Jones, A.E., 2014. Hydrothermal transport and precipitation of the rare earth elements by fluorine-bearing aqueous liquids. Miner. Depos. 49, 987–997.

Möller, P., Parekh, P.P., Schneider, H.J., 1976. The application of Tb/Ca–Tb/La abundance ratios to problems of fluorspar genesis. Miner. Depos. 11, 111–116.

Putnis, A., 2002. Mineral replacement reactions: from macroscopic observations to microscopic mechanisms. Mineral. Mag. 66 (5), 689–708.

Putnis, A., 2009. Mineral replacement reactions. Rev. Mineral. Geochem. 70 (1), 87–124.

Sallet, R., Moritz, R., Fontignie, D., 2005. The use of vein fluorite as probe for paleofluid REE and Sr–Nd isotope geochemistry: the Santa Catarina Fluorite District, Southern Brazil. Chem. Geol. 223 (4), 227–248.

Samson, I.M., Wood, S.A., 2005. The rare earth elements: behavior in hydrothermal fluids and concentration in hydrothermal mineral deposits, exclusive of alkaline settings In: Linnen, R.L., Samson, I.M. (Eds.), Rare-element Geochemistry and Mineral Deposits, Geological Association of Canada, GAC Short Course Notes. 17, pp. 269–297.

Schlegel, T.U., Wagner, T., Fusswinkel, T., 2020. Fluorite as indicator mineral in iron oxide-copper-gold systems: explaining the IOCG deposit diversity. Chem. Geol. 548, 119674.

Schönenberger, J., Köhler, J., Markl, G., 2008. REE systematics of fluorides, calcite and siderite in peralkaline plutonic rocks from the Gardar Province. South Greenland. Chemical Geology. 247 (1-2), 16–35.

Schwinn, G., Markl, G., 2005. REE systematics in hydrothermal fluorite. Chem. Geol. 216 (3-4), 225–248.

Sheard, E.R., Williams-Jones, A.E., Heiligmann, M., Pederson, C., Trueman, D.L., 2012. Controls on the Concentration of Zirconium, Niobium, and the Rare Earth Elements in the Thor Lake Rare Metal Deposit, Northwest Territories. Canada. Econ. Geol. 107 (1), 81–104.

Shu, X., Liu, Y., Li, D., 2020. Fluid inclusions as an indicator for REE mineralization in the Lizhuang deposit, Sichuan Province. Southwest China. J. Geoche. Explor. 213, 106518.

Simandl, G.J., Paradis, S., 2018. Carbonatites: related ore deposits, resources, footprint, and exploration methods. Appl Earth Sci. 127 (4), 123–152.

Smith, M.P., Henderson, P., 2000. Preliminary fluid inclusion constraints on fluid evolution in the Bayan Obo Fe-REE-Nb deposit, Inner Mongolia. China. Econ. Geol. 95, 1371–1388.

Trofanenko, J., Williams-Jones, A.E., Simandl, G.J., Migdisov, A.A., 2016. The nature and origin of the REE mineralization in the Wicheeda Carbonatite, British Columbia. Canada. Econ. Geol. 111 (1), 199–223.

Verplanck, P.L., Mariano, A.N., Mariano, A., 2016. Rare Earth and Critical Elements in Ore Deposits. Society of Economic Geologists.

Walter, B.F., Steele-MacInnis, M., Markl, G., 2017. Sulfate brines in fluid inclusions of hydrothermal veins: Compositional determinations in the system H2O-Na-Ca-Cl-SO4. Geochim. Cosmochim. Acta. 209, 184–203.

Walter, B.F., Steele-MacInnis, M., Giebel, R.J., Marks, M.A.W., Markl, G., 2020. Complex carbonate-sulfate brines in fluid inclusions from carbonatites: Estimating compositions in the system H2O-Na-K-CO3-SO4-Cl. Geochima. Cosmochim. Acta. 277, 224–242.

Wan, Y.e., Wang, X., Chou, I.-M., Li, X., 2021. Role of sulfate in the transport and enrichment of REE in hydrothermal systems. Earth Planet. Sci. Lett. 569, 117068.

Wang, J.-H., Yin, A.n., Harrison, T.M., Grove, M., Zhang, Y.-Q., Xie, G.-H., 2001. A tectonic model for Cenozoic igneous activities in the eastern Indo-Asian collision zone. Earth Planet Sc Lett 188 (1-2), 123–133.

Williams-Jones, A.E., Palmer, D.A.S., 2002. The evolution of aqueous-carbonic fluids in the Amba Dongar carbonatite, India: implications for fenitization. Chem. Geol. 185, 283–301.

Xie, Y., Hou, Z., Yin, S., Dominy, S.C., Xu, J., Tian, S., Xu, W., 2009. Continuous carbonatitic melt–fluid evolution of a REE mineralization system: evidence from inclusions in the Maoniuping REE Deposit, Western Sichuan. China. Ore Geol. Rev. 36 (1-3), 90–105.

Xu, C., Taylor, R.N., Li, W., Kynicky, J., Chakhmouradian, A.R., Song, W., 2012. Comparison of fluorite geochemistry from REE deposits in the Panxi region and Bayan Obo. China. J. Asian Earth Sci. 57, 76–89.

Yin, A.n., Harrison, T.M., 2000. Geologic evolution of the Himalayan-Tibetan orogen. Annu. Rev. Earth Planet. Sci. 28 (1), 211–280.

Yuan, Z.X., Shi, Z.M., Bai, G., Wu, C.Y., Chi, R.A., Li, X.Y., 1995. The Maoniuping Rare Earth Ore Deposit, Mianning County, Sichuan Province, 150 p. Seismological Publishing House, Beijing (in Chinese).

Zhang, W., Chen, W.T., Mernagh, T.P., Zhou, L.i., 2022. Quantifying the nature of ore-forming fluids in the Dalucao carbonatite-related REE deposit, Southwest China: implication for the transport and deposition of REEs. Miner. Depos. 57 (6), 935–953.

Zhang, Y., Liu, Y., Hou, Z., Zheng, X.u., 2021. Iron and sulfur isotopic compositions of carbonatite-related REE deposits in the Mianning–Dechang REE belt, China: Implications for fluid evolution. Ore Geol. Rev. 138, 104373.

Zheng, X., Liu, Y., Ou, Y.H., Fu, H.B., Jia, Y.H., Ding, Y., 2019. The evolution of ore-forming fluid constraints on mineralization of the Muluozhai carbonatite-related REE deposit in western Sichuan: Evidence from fluid inclusions and stable isotopes. Acta Petrologica Sinica. (in Chinese).

Zheng, X., Liu, Y., 2019. Mechanisms of element precipitation in carbonatite-related rare-earth element deposits: Evidence from fluid inclusions in the Maoniuping deposit, Sichuan Province, southwestern China. Ore Geol. Rev. 107, 218–238.

Zheng, X.u., Liu, Y., Zhang, L., 2021. The role of sulfate-, alkali-, and halogen-rich fluids in mobilization and mineralization of rare earth elements: Insights from bulk fluid compositions in the Mianning–Dechang carbonatite-related REE belt, southwestern China. Lithos. 386-387, 106008.

Zhong, D.L., Ding, L., Liu, F.T., Liu, J.-H., Zhang, J.J., Ji, J.-Q., Chen, H., 2001. The multidirection layer and frame structure of rock layers in orogenic belt and its control on Cenozoic magmatic activities: an example from Sanjiang and its neighboring area. Sci. China 30, 1–8 in Chinese.